Project Number: ZWH-AA2N

WPI

University of Massachusetts
UMASS Medical School

Brain SPECT Collimator Design

A Major Qualifying Project Report: Submitted to the Faculty of
WORCESTER POLYTECHNIC INSTITUTE
in partial fulfillment of the requirements for the
Degree of Bachelor of Science
By

Yulun He _____

Submitted:
April 27, 2017

Approved by Professors Zhikun Hou and David Medich, Project Advisors

_____

Abstract

A multi-pinhole (MPH) collimator is designed to pair with an existing fan-beam collimator for single-photon emission computed tomography (SPECT). A mechanical design has been developed for constructing a brain-dedicated MPH collimator that will replace a commercial single pinhole collimator for general imaging. The spatial and weight constraints are satisfied. Material deformation during operation is simulated and used to ensure safety and imaging accuracy. Monte-Carlo simulation of the gamma-ray interaction is performed to simulate brain imaging and validate the model geometry. The student has also determined the operation type of the shutter mechanism for specific apertures that will allow or restrict the passage of photons to adapt the imaging characteristics of the collimator.

Disclosure & Acknowledgements

The project is a portion of the research under the collaboration of University of Massachusetts Medical School, University of Arizona, and Z-Concepts, LLC. Research reported in this publication was supported by the National Institute of Biomedical Imaging and Bioengineering of the National Institutes of Health under Awards R21 EB016391 and R01 EB022092. The content is solely the responsibility of the authors and does not necessarily represent the official views of the National Institutes of Health.

I would like to express my deepest appreciation to my academic advisors Professors Zhikun Hou in Mechanical Engineering and David Medich in Physics for their guidance throughout my years of undergraduate study that have allowed me to obtain a double major in Mechanical Engineering and Physics, as well as to successfully complete the MQP.

I would also like to thank Professor Richard Sisson in Mechanical Engineering for his generous help in helping me find the tensile testing machine that I need to use to test the mechanical properties of the materials that will be used to build the system. Furthermore, many thanks to Dr. Yangzi Xu for helping using the tensile machine of her lab and to Russell Lang in Civil Engineering for his teaching me and allow me to use the tensile testing machine.

Finally, I would like to give my special gratitude to Dr. Michael King at the University of Massachusetts Medical School for the precious opportunity to participate in the imaging research and turn it into a project and his advice and guidance for my career in medical physics. I would also like to thank Dr. Arda Könik, Dr. Kesava Kalluri and the rest of the group members for helping me to complete the project.

Table of Contents

1 INTRODUCTION 1

1.1 BACKGROUND REVIEW 1

1.1.1 Parkinson's Disease 1

1.1.2 SPECT and Its Application in Brain Imaging 2

1.1.3 SolidWorks 7

1.1.4 GATE 8

1.1.5 Photon Attenuation in Matter 9

1.2 OBJECTIVE 11

2 APPROACH 12

2.1 INDIVIDUAL COMPONENT DESIGN PROCESS 12

2.1.1 XCAT Phantom 12

2.1.2 Commercial single pinhole collimator 13

2.1.3 Crystalline Detector of Camera 14

2.1.4 Collimator plate 14

2.1.4.1 Plate Size and Material 15

2.1.4.2 Multi-Pinhole Design 16

2.1.4.3 Multiplexing Pinholes 18

2.1.5 Side Shields 19

2.1.6 Shutter Mechanism 21

2.1.6.1 Shutter Block 22

2.1.6.2 Shutter Tracks 24

2.1.6.3 Air-Piston/Spring Mechanism (Curved) 24

2.2 ASSEMBLING PROCESS 27

2.3 VALIDATION 30
2.3.1 Spatial Constraint 30
2.3.2 Weight Constraint 32
2.3.3 Deformation 33
2.3.4 GATE 38
3 CONCLUSION 41
4 DISCUSSION 42
4.1 COMPONENT ATTACHING PROCESS 42
4.2 SHUTTER MECHANISM 42
4.3 GATE RESULT 45
5 REFERENCES 48

i. List of Figures

Figure 1. Locations of substantia nigra, caudate, and putamen (Challenged, 2015). 2

Figure 2. SPECT Images with DaTscan™ 3

Figure 3. Philips BrightView - XCT SPECT System (Philips, 2017). 4

Figure 4. Cross-sectional view of a (a) parallel-hole collimator (b) fan beam collimator (c) pinhole collimator. 5

Figure 5. (A) An MRI image showing the cross-sectional view of putamen, caudate, and region of occipital lobe labeled (source: John Seibyl MD, Molecular NeuroImaging LLC) (B) A current standard SPECT I-123 DaTScan that is unable to separate putamen and caudate (M. A. King, 2016) 6

Figure 6. Overlapping projections in a multiplexing multiple-pinhole system (Karen Van Audenhaege, 2015). 7

Figure 7. GATE Environment..... 8

Figure 8. Isotropic view of the XCAT phantom 12

Figure 9. Philips commercial single pinhole collimator 13

Figure 10. SolidWorks model of the Philips commercial single pinhole. 14

Figure 11. SolidWorks model of crystal model. 14

Figure 12. Front view (top) and side view (bottom) of the two loft geometries..... 16

Figure 13. Side view of collimator plate demonstrating the location of VOI..... 17

Figure 14. Lofted Cut with larger circle 4 cm above the aperture. 18

Figure 15. Top view of collimator plate only showing 3 x 3 pinholes. 18

Figure 16. Top view of collimator plate also showing multiplexing pinholes. 19

Figure 17. Larger loft to create side shields. 20

Figure 18. (a) Before collimator plate volume is removed (b) cross-sectional view of the loft after center cavity is removed 20
Figure 19. (a) back shield (b) front shield (c) left shield (d) right shield. 21
Figure 20. Bottom view of the aperture plate in the assembly showing the created shutter mechanism for the most oblique additional pinhole for multiplexing that is highlighted in blue. 22
Figure 21. Isotropic view of the shutter. 23
Figure 22. Cross-sectional view of the collimator plate and shutter. This view only shows one extension for the track because the extensions are not created on the same plane with each together due to the elliptical shape of the shutter. 23
Figure 23. Cross-sectional view of the two shutter tracks. 24
Figure 24. Dimension of the two shutter extensions which is replicated on the tracks. 24
Figure 25. The bottom view of the collimator plate showing the air tube, the piston, and the spring 25
Figure 26. (a) Spring is contracted and the pinhole is open. (b) Spring is stretched and the pinhole is shut. 25
Figure 27. Cross-sectional view of air tube. 26
Figure 28. (a) Piston in the air tube (b) Spring highlighted in blue. 26
Figure 29. Side view of the MPH collimator demonstrating the distance from the crystal to the aperture level 27
Figure 30. Cross-sectional view of the assembly 28
Figure 31. Assembly process of the collimator plate with the four shields (base and crystal not shown). 28

Figure 32. Side Skirts are highlighted in blue. 29
Figure 33. Complete view of the collimator system with XCAT phantom added. The dashed line indicates the axial direction of the phantom which is also what the MPH collimator rotates about. 29
Figure 34. Distance between direct pinhole and the back end of the collimator. 30
Figure 35. (a) Coronal view of the XCAT Phantom (b) Transverse view of the XCAT Phantom. 31
Figure 36. Collimator cart carrying the commercial single pinhole collimator. 31
Figure 37. (a) Cart Mockup (purple) (b) intersection between the right shield of the MPH collimator and the collimator cart, highlighted in red oval in (a). 32
Figure 38. SolidWorks drawing of the tensile testing specimen design. 33
Figure 39. Two sets of specimens: tungsten alloy and lead alloy. For each set, the upper one is the tested and the lower one is the unused. 34
Figure 40. Stress-strain curve of two tungsten alloy specimens. 34
Figure 41. Stress-strain curve of four lead alloy specimens. 35
Figure 42. Stress-strain curve of tested tungsten alloy by the testing company. 36
Figure 43. Tested mechanical properties of the two specimens 36
Figure 44. MPH collimator in GATE. 39
Figure 45. GATE simulation result of the additional eight pinholes for multiplexing (top three) and the original nine pinholes (bottom three). 39
Figure 46. GATE simulation results for multiplexing, red: original nine pinholes & green: additional eight pinholes. 40
Figure 47. One attaching surface. 42

Figure 48. The change of relative postiion of the piston tip with respect ot the track direction of the shutter. 43
Figure 49. Potential blockage of the adjacent pinhole by the air piston. 43
Figure 50. The other additional pinhole of the same column circled in red. 44
Figure 51. Shutter for the direct pinhole (a) top view with the entire collimator plate shown (b) isotropic view. 44
Figure 52. Low count issue in GATE circled in red. 45
Figure 53. GATE simulation result of the additional pinholes with a point source. The chart in the lower image demonstrates the counts at the corresponding pinholes from the region selected in the yellow rectangle in the upper image. 46
Figure 54. (a) Previous model of only original pinholes (b) GATE image of the model. 46
Figure 55. Potential unsymmetrical meshing. 47

ii. List of Abbreviations

PD	Parkinson’s Disease
SPECT	Single Photon Emission Computed Tomography
CT	Computed Tomography
MRI	Magnetic Resonance Imaging
MPH	Multi-Pinhole
GATE Geant4	Application for Emission Tomography
XCAT	4D Extended Cardiac-Torso
FEA	Finite Element Analysis
SW	SolidWorks
FWHM	Full-Width-at-Half-Maximum
PSF	Point Spread Function
VOI	Volume of Interest

1 Introduction

1.1 Background Review

1.1.1 Parkinson's Disease

The human brain is a well-optimized organ that allows us to think and move as a person. However, due to aging and other factors, some brain disorders, such as Parkinson's Disease, are unavoidable. Parkinson's Disease (PD) is a long-term degenerative disorder of the central nervous system that causes a loss of motor control. According to the Parkinson's Disease Foundation, currently there are about 1 million people in the US and 10 million worldwide living with PD. There is no cure to the disease, and procedures such as medications and surgeries can only alleviate the symptoms caused by the disease. However, early detection of the disease-type indications has become crucial for correct diagnosis of PD to allow the patients symptoms to be managed. It is also needed so that patients with different diseases that manifest clinically similarly to PD will not be incorrectly managed as having PD with the possibility of side-effects with no benefits, and can instead be treated for their actual disease.

PD can first be detected by the degeneration of neurons that produce the neurotransmitter dopamine in the substantia nigra. The dopamine produced from the nigra is released into two structures of the midbrain, the putamen and caudate, which together are referred to as the striatum. Figure 1 below illustrates the locations of these structures.

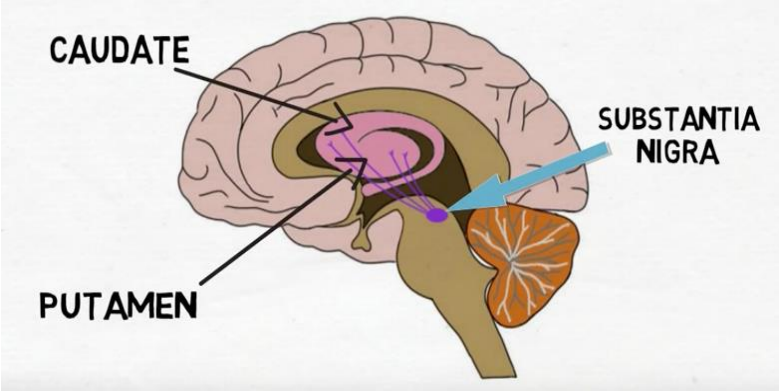

Figure 1. Locations of substantia nigra, caudate, and putamen (Challenged, 2015).

The striatum is found to play an important role in movement control. Therefore, the clear imaging of striatum function is crucial to identifying PD and determining its progression. One way to achieve this is through SPECT imaging.

1.1.2 SPECT and Its Application in Brain Imaging

Single photon emission computed tomography (SPECT) is a medical imaging technique that demonstrates the functionality of the body as compared to the anatomical configuration presented by computed tomography (CT) or magnetic resonance imaging (MRI). To achieve this, radionuclide tracers that emit high energy photons, known as gamma-rays, are attached to a selected molecule to yield an imaging agent which is injected into the bloodstreams of patients. This substance will participate in the body's metabolism and accumulate uptake at sites specific to the imaging agent. For example, Technithium-99m labeled to different molecules is widely used for imaging thyroid carcinoma, inflammation and cerebral perfusion imaging (Giuliano Mariani, 2010). As these radionuclides decay, gamma-rays will be emitted randomly in all directions and exit the body to be detected by a gamma camera. A collimator eliminates the

photons that are not aligned with the prescribed open paths to the camera's detector. In essence, the collimator acts as the lens of the for the system. By matching the site of detection with the prescribed path, reconstruction is able to trace back the trajectory and reconstruct the original three-dimensional distribution of the source.

Figure 2 below is a set of brain images that compare a normal striatum and a diseased striatum. These images are generated with DaTscan™, an FDA-approved imaging agent for the assessment and diagnosis of PD developed by GE Healthcare. It uses I-123 as the radionuclide

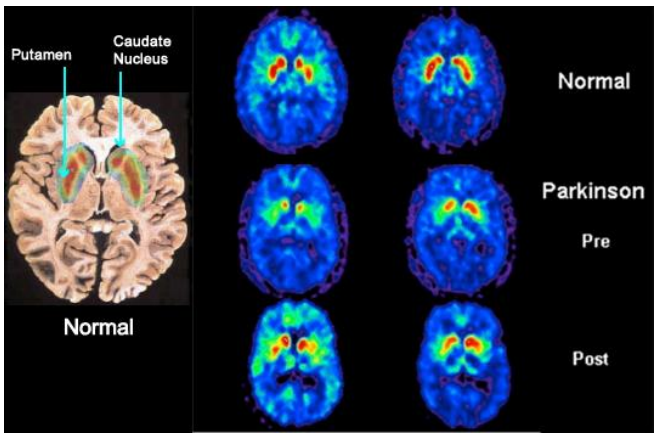

Figure 2. SPECT Images with DaTscan™

tracer. Such images are generated through a component of SPECT called the collimator. In clinical systems, the collimator is mounted on the camera head. Figure 3 below is the Philips BrightView SPECT system which the collimator of this project is designed to image with. The two camera heads are aligned with each other. When the patient is moved in between the heads, the gamma-rays leave the body, pass through the collimators, and interact with the detectors located at the back of the camera head.

Figure 3. Philips BrightView - XCT SPECT System (Philips, 2017).

There are three common types of collimators employed clinically: fan beam, parallel hole, and multi-pinhole. Figure 4 below shows the simple configurations of these three collimators (Karen Van Audenhaege, 2015). The parallel-hole collimator is the most common standard collimators for clinical practice. It consists of honeycomb shaped, closely packed holes made of high-density materials, usually lead mixed with antimony. Only photons with trajectory parallel to the holes have the highest chance of reaching the detector. One advantage of the parallel-hole collimator is the large field-of-view. Another type of collimator is converging collimator. When the object is smaller than the available detector area, a converging collimator, whose hole directions focus to a point, is used to maximize the usage of detector area and improve resolution. For this reason, clinical brain imaging usually uses fan-beam collimator. The third type of collimator, although less commonly used, is a pinhole collimator that consists of one or more apertures made of tungsten or other high-density materials. Pinhole collimators provide relatively high resolutions with the sacrifice of sensitivity. However, this can be compensated by adding multiple pinholes to allow more photons to register on the detector on the other end.

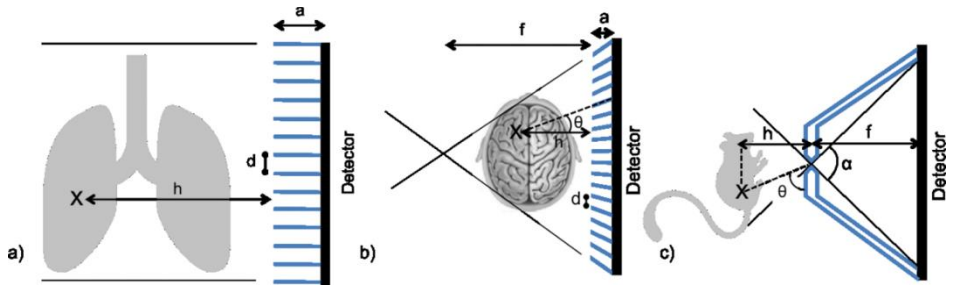

Figure 4. Cross-sectional view of a (a) parallel-hole collimator (b) fan beam collimator (c) pinhole collimator.

Two important system properties of SPECT imaging are spatial resolution and sensitivity. Sensitivity is also known as detection efficiency. Spatial resolution reflects the sharpness or detail of the image. It is quantified by the full-width-at-half-maximum (FWHM) of the point spread function (PSF). Sensitivity is a measurement of the number of detected versus emitted photons.

SPECT imaging has been extensively used to diagnosis brain disorders. Parkinson's disease, "a progressive neurodegenerative condition resulting from the death of the dopamine containing cells of the substantia nigra" (Conditions, 2006), is of interest in this research. In 2011, the Food and Drug Administration (FDA) approved SPECT imaging agent I-123 labeled DaTscan for diagnosis and progression monitoring of the disease. For this agent, the volume of interest (VOI) is the center of the brain where the functional activity of caudate and putamen are to be analyzed. Figure 5 below shows the location of the structures inside the brain and a sample SPECT image acquired.

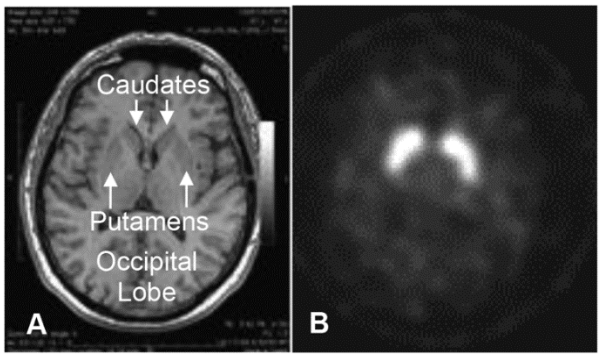

Figure 5. (A) An MRI image showing the cross-sectional view of putamen, caudate, and region of occipital lobe labeled (source: John Seibyl MD, Molecular NeuroImaging LLC) (B) A current standard SPECT I-123 DaTScan that is unable to separate putamen and caudate (M. A. King, 2016)

From Figure 5, it is clear that proper evaluation and diagnosis of PI requires the imaging system to be able to distinguish the two lobes of the Occipital organ. To that end, our research group has proposed to substitute one of the existing fan-beam collimator on the Philips BrightView system with a MPH collimator with enhanced spatial resolution and sensitivity. This gives the advantage of producing sharp image within the VOI by the MPH collimator, with the fan-beam collimator completing the background with complete sampling of the brain.

The uptake pattern of the gamma rays can vary with patient and time after agent injection. Thus, the development of a collimator that can adapt to the patient by altering the number and size of the apertures letting photons pass through would be of significant utility clinically. Multiplexing represents the allowing of photons detected at a given location to have passed through more than one aperture in the collimator. As Figure 6 illustrates, there is an overlapping region of the field of view of the two pinholes.

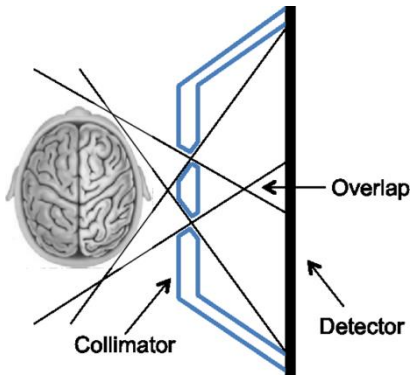

Figure 6. Overlapping projections in a multiplexing multiple-pinhole system ***(Karen Van Audenhaege, 2015)****.*

Any photon registration in this region can be traced back through either pinhole if filtered back projection is used for reconstruction. Multiplexing can increase sensitivity by adding more events to the data used in reconstruction, but has the potential to reduce image quality through the creation of artifacts. As a result, temporal alteration of multiplexing during acquisition has been proposed as a method of avoiding artifact production, while gaining the benefit of the added counts. Hence, the design of a collimator that can vary multiplexing temporally is of interest to be explored.

1.1.3 SolidWorks

In this study, we used the SolidWorks program to model our proposed imaging system. SolidWorks is a solid modeling software that allows the user to implement computer-aided design (CAD). It also provides simulation for engineering purposes. For this project, SolidWorks was used to create the preliminary mechanical design to visualize, finite-element analysis of the spatial deformation of the collimator, and input the geometry of the collimator into GATE package to simulation SPECT imaging result.

1.1.4 GATE

GATE (Geant4 Application for Tomographic Emission) is an open-source software developed by the international OpenGATE collaboration and is dedicated to numerical simulations in medical imaging and radiotherapy (S Jan, 2004). It provides realistic simulation of radionuclide decay. It is an interactive add-on to GEANT Monte Carlo package which uses Monte Carlo methods to simulate particle passages through matter, more specifically the interactions of gamma-rays in patients and imaging systems. A phantom can be defined with a source distributed throughout a region. The activity, acquisition time, and other parameters can be specified.

In the initialization process of GATE, the user needs to define the scanner geometry, define the phantom geometry, define the physics processes, and initialize the simulation. The Figure 7 below demonstrates the GATE environment. The largest and the second largest cubes

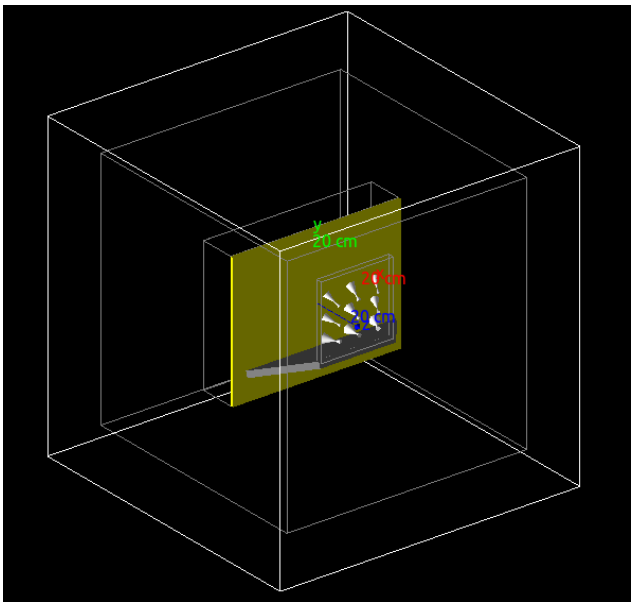

Figure 7. GATE Environment

indicate the world volume that all the components are created within and the scanner volume, which, in the case of this research, is the MPH SPECT machine volume and is a subset to the world volume. The phantom (not shown) is a subset that is directly underneath the world volume, sharing the same hierarchy as the scanner volume. Within the scanner volume, individual collimator components are defined: in the above picture, the transparent collimator plate consisting nine pinholes, the side shield shown in gray, and the crystalline detector shown in yellow. The physics process within the phantom is essentially the distribution of the source, the type of source, and the activity of the source (the rate at which the source decays). The acquisition time is then defined to set the time limit till when the simulation stops and then generates an image.

1.1.5 Photon Attenuation in Matter

Photons deposit energy in matter mainly through three mechanisms: photoelectric effect, Compton scatter, and pair production. The ejection of electrons from an atom as a result of the absorption of photons (electromagnetic radiation) is called the photoelectric effect. During this process, an ionizing photon interacts with an atomic electron causing the electron to become a free electron. In Compton scatter, a photon of initial energy E interacts with an atomic electron. During this interaction, the photon transmits part of its energy to the electron. The electron becomes ionized (free) with a kinetic energy ($E - E' – E_0$, where E_0 is the binding energy of the electron) and the "new" photon, which now has an energy E' travel in directions dictated by Conservation of Momentum. A photon with an energy of at least twice the electron rest energy, $h\nu \geq 2mc^2$, can be converted into an electron–positron pair in the field of an atomic nucleus. Pair

production can also occur in the field of an atomic electron, but the probability is considerably smaller and the threshold energy is $4mc^2$.

The distance of photon travels within a material is governed statistically by a probability of interaction per unit distance traveled, which depends on the specific medium traversed and on the photon energy. This probability, named the linear attenuation coefficient (LAC) (or macroscopic cross section), is symbolized by μ and has the dimensions of inverse length (e.g., cm^{-1}). The mass attenuation coefficient is another way of representing the LAC. It is obtained by dividing μ by the density ρ of the material, and is usually expressed in cm^2g^{-1}. It represents the probability of an interaction per $cm^{-2}g$ of material traversed (Turner, 2007). For instance, when a beam of N_0 monoenergetic photons incident normally on a slab, we let N(x) represent the number of photons that reach a depth x without having interacted. The number that interact within the next small distance dx is proportional to N and to dx by the LAC. Thus, we may write $dN = -\mu N dx$ which leads to $N(x) = e^{-\mu x}N_0$, or $\frac{N(x)}{N_0} = e^{-\mu x}$ where $e^{-\mu x}$ is the probability that a photon will traverse a distance x without interacting with the material, in other words, the fraction of the remaining photon after traveling a distance x. Hence, a large LAC will yield a low fraction of remaining.

The LAC is inversely correlated to incident photon energy but positively correlated to the density of the material. For a SPECT collimator, in order to eliminate as much the unwanted photons as possible that will likely disturb the imaging quality, a high-density and atomic number material must be selected to construct the collimator. Lead and tungsten are commonly used and are candidates for the material selection of our MPH collimator.

1.2 Objective

The current state-of-the-art of SPECT imaging has yet to specialize brain imaging. The objective of the project is therefore to design an MPH collimator, altered from a commercial single pinhole collimator, that can be added to the second head of the Philips BrightView SPECT system which will enable combined enhanced spatial resolution and sensitivity imaging of the VOI (volume of interest) for DaTscan imaging, and employ multiplexing to further increase the sensitivity of imaging. The apertures of the collimator are designed to focus on viewing the striatum region of the brain.

To achieve this goal, the following tasks were performed: a preliminary mechanical design of the collimator system that can image striatum and putamen of patients with Parkinson's disease as well as shutter mechanism to allow multiplexing was developed using the SolidWorks program, and the GATE simulations program was used to simulate and test imaging quality and photon penetration through shields for these designs.

2 Approach

2.1 Individual Component Design Process

2.1.1 XCAT Phantom

A computational phantom of human anatomy is used in the project to validate the spatial feasibility of the design through visualizing a virtual model of the patient's anatomy in the system. Figure 8 below shows a wire mesh rendering of the surface of an XCAT phantom that provides an accurate representation of the human body (W. P. Segars, 2010). Here only head, upper torso, two upper arms with shoulders are used relative to the interest of this research. Based on estimated location, the student combine the torso, head, and two arms together as a single assembly.

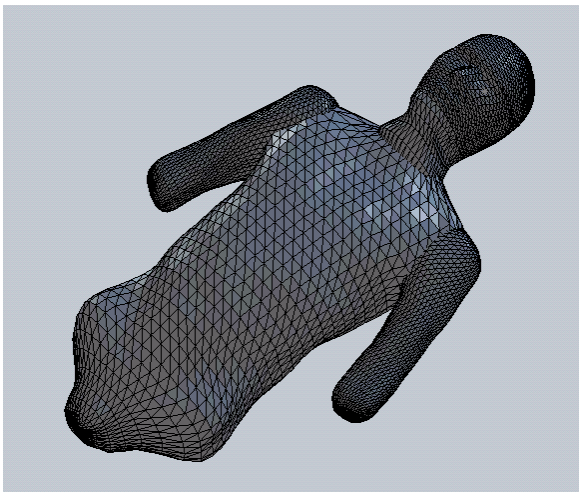

Figure 8. Isotropic view of the XCAT phantom

2.1.2 Commercial single pinhole collimator

The mockup of the current commercial single pinhole collimator, shown in Figure 9, is obtained from Philips. It will become the base that supports the MPH collimator. It is made of 95% lead and 5% antimony. It is modeled from the official SolidWorks drawing from Philips and is shown in Figure 10. The conical portion in the center indicates the single pinhole structure which will be cut and replaced by the new MPH configuration. This detailed procedure will be explained in Assembling Process later.

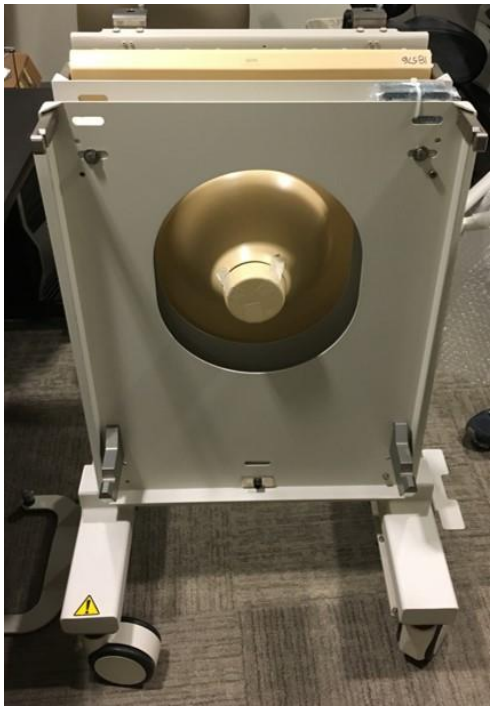

Figure 9. Philips commercial single pinhole collimator

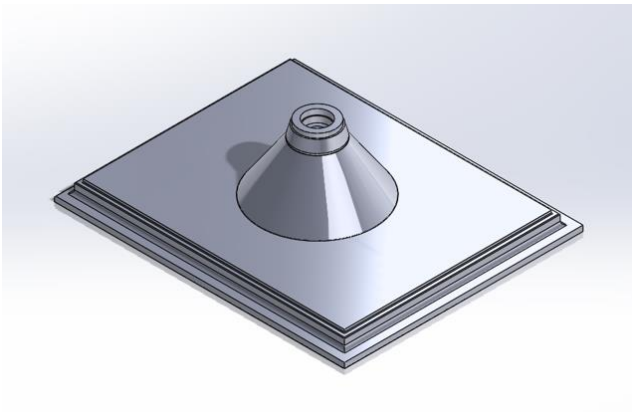

Figure 10. SolidWorks model of the Philips commercial single pinhole.

2.1.3 Crystalline Detector of Camera

Demonstrated by Figure 11 below, the crystal is modeled to duplicate the crystals on the

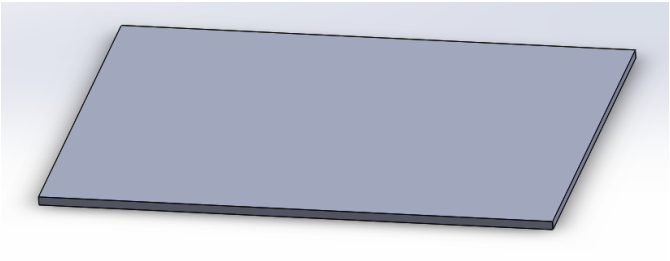

Figure 11. SolidWorks model of crystal model.

current Philips BrightView XCT system. The flat surface has a dimension of 560 mm x 438 mm x 9.5 mm. It is created from a simple extrude.

2.1.4 Collimator plate

The collimator plate is the plate parallel to the detector and blocks the portion of the gamma rays that do not follow the prescribed path of the pinholes.

2.1.4.1 Plate Size and Material

The desired thickness of the collimator plate is determined is determined as that which will attenuate the low-abundance high-energy photons of I-123 sufficiently so they are at or below the level they are present in clinical studies with pinhole collimators. A low fraction indicates the collimator plate is able to eliminate a large number of incident gamma rays. Lead-antimony alloy (94%+6%) and tungsten-nickel-copper alloy (90%+6%+4%) are two candidates for the collimator system. The two most abundant gamma ray energies emitted by I-123 are the 159 keV primary photons and 529 keV secondary photons (David A. Weber, 1989). The NIST XCOM database (Technology, n.d.) is used to obtain the mass attenuation coefficients for these two materials and two photon energy levels. These values can then be converted to linear attenuation coefficients through multiplying by the densities of the materials obtained from CES EduPack. Table 1 below documents the calculated LACs for the four energy-material combinations.

Table 1. Linear attenuation coefficients for lead and tungsten at specific energies of interest.

LAC [cm^{-1}]	Pb-Sb (10.9 g/cm^3)	W-Ni-Cu (17 g/cm^3)
159 keV	1.82E+01	2.13E+01
529 keV	1.45E+00	2.10E+00

The primary photon does not require much thickness due to its high LAC–for a thickness of 2 cm lead slab, the fraction of these 159 keV photons that are remained is 1.55E-16. Therefore, the main focus is on the secondary photons as it is more penetrating as compared to the primary. For the same thickness, the remaining photons take up the fraction of 5.50% and 1.50% for the two materials, respectively. Although the number 1.50% is above 1%, the abundancy of the

secondary gamma ray is low enough (about 1.4%) to compensate for this. Therefore, the group selected material 2 cm thick tungsten alloy for the collimator plate.

The collimator plate is modeled with two Lofted Cut features forming two stacked flat pyramids that are each 1 cm thick. The bottom pyramid secures the plate and locks it with the side shields that are discussed in the next section. It is symmetric along the sagittal direction. The upper loft has top surface to be 157 mm x 250 mm and bottom surface to be 265.91 mm x 171.28 mm. The latter surface is determined by enlarging the top surface along two lines for each side view. This surface also serves to create the top surface of the lower loft through enlarging the rectangle. The bottom surface of the lower loft is created in a similar fashion with its counterpart in the upper loft. The design scheme is illustrated in Figure 12 below.

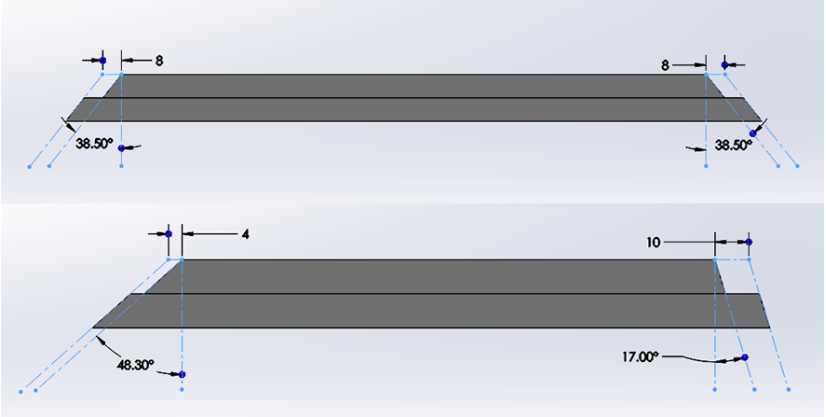

Figure 12. Front view (top) and side view (bottom) of the two loft geometries.

2.1.4.2 Multi-Pinhole Design

The volume of interest (VOI) of the system is a cylinder with diameter 12.0 cm and height 8 cm that is aligned axially to simulate the center region of the brain (M. A. King, 2016).

For simulation purposes, it is represented by a point source that is 14 cm above the aperture level shown in Figure 13.

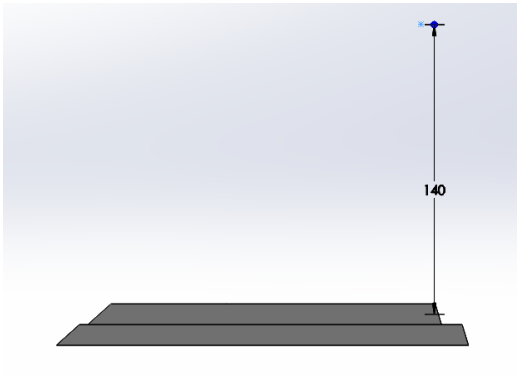

Figure 13. Side view of collimator plate demonstrating the location of VOI.

The group has determined to use a 3 x 3 arrangement of the aperture with the diameter of 2.5 mm. They are 0.5 cm below the top surface of the collimator plate. Each pinhole faces the VOI. Therefore, the plane that each aperture circle lies on is determined by connecting a straight line between the aperture center and the VOI, and making the plane perpendicular to this line at the aperture center. Pinhole cavities are created with mirrored Lofted Cut features. A plane that is parallel and 4 cm above the aperture plane. As Figure 14 below shows, a larger circle of a given size is provided and the loft-cut can be performed to create the upper cavity.

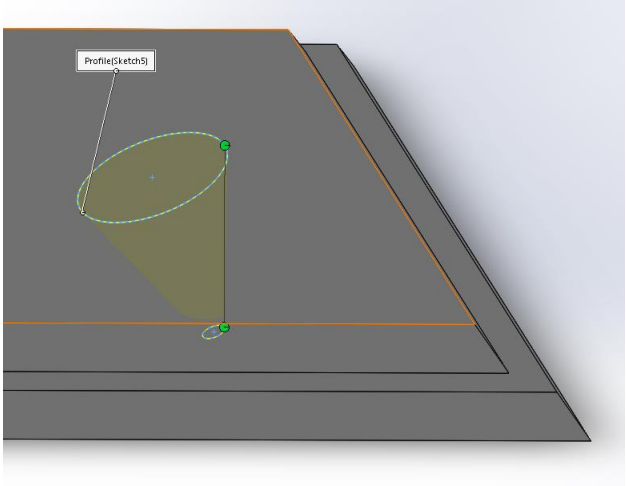

Figure 14. Lofted Cut with larger circle 4 cm above the aperture.

The lower cavity is obtained from mirroring the upper cavity about the aperture plane. Figure 15 below shows the apertures colored in green. The bottom center aperture that directly faces the viewer is the direct pinhole as it is directly underneath the VOI in the side view.

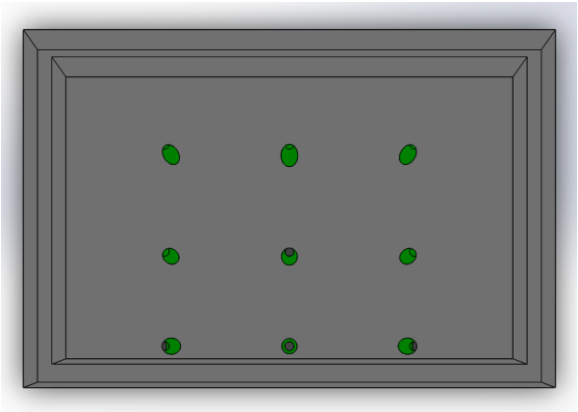

Figure 15. Top view of collimator plate only showing 3 x 3 pinholes.

2.1.4.3 Multiplexing Pinholes

In order to better utilize the detector region, multiplexing pinholes are added as Figure 16 below shows. They are created in the same way as the regular pinholes.

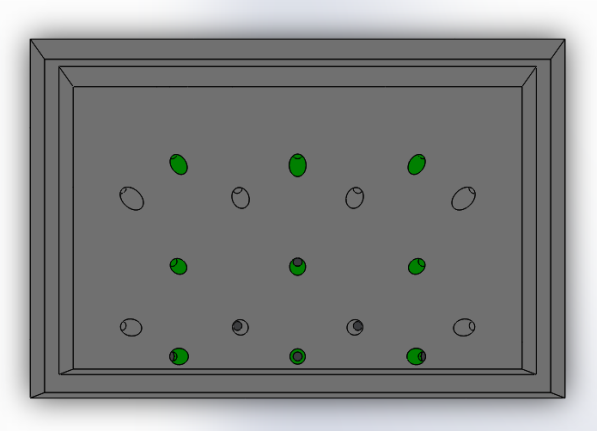

Figure 16. Top view of collimator plate also showing multiplexing pinholes.

2.1.5 Side Shields

The function of the side shields is to provide shielding surrounding the aperture plate to prevent unwanted photons from body regions other than the brain and background radiation to register on the detector, which will deteriorate the image quality by introducing artifacts. The material has been chosen as the tungsten alloy for its higher strength compared to the lead alloy. This minimizes the thickness for the same penetration fraction of gamma rays, which leaves as much of the existing collimator intact to not compromise much of its integrity when cut. This ensures a strong support of the MPH collimator. This also maximizes the usable detecting area of the crystalline detector for the outer-edge pinholes. The side shields are created from a larger loft, shown in Figure 17 that follows the same angled guiding lines as the collimator plate and is also symmetric along the sagittal direction.

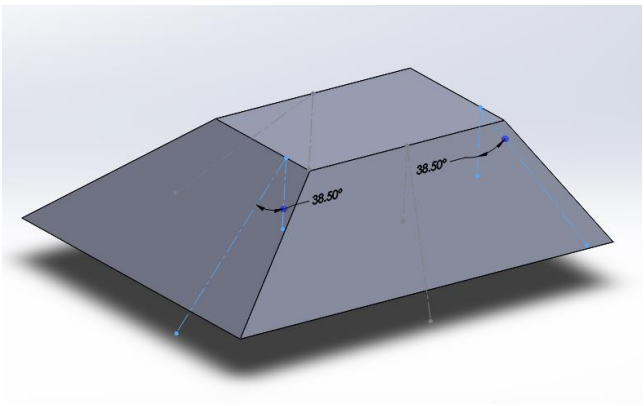

Figure 17. Larger loft to create side shields.

The collimator plate is then placed inside this geometry with both top surfaces coincident with each other. The volume of the aperture is cut out from the larger loft. Another volume is removed by tracing the guide lines of the lower loft of the collimator plate. This step can be seen in Figure 18 below.

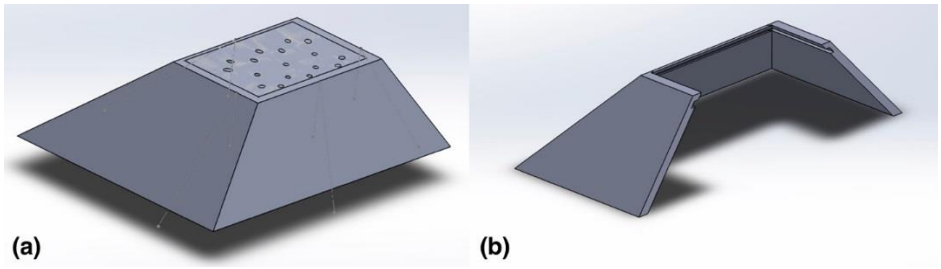

Figure 18. (a) Before collimator plate volume is removed (b) cross-sectional view of the loft after center cavity is removed

Finally, four shields are cut from the remaining geometry of the larger loft as shown in Figure 19 below. The shape of the edges enables each shield to lock with its adjacent shields.

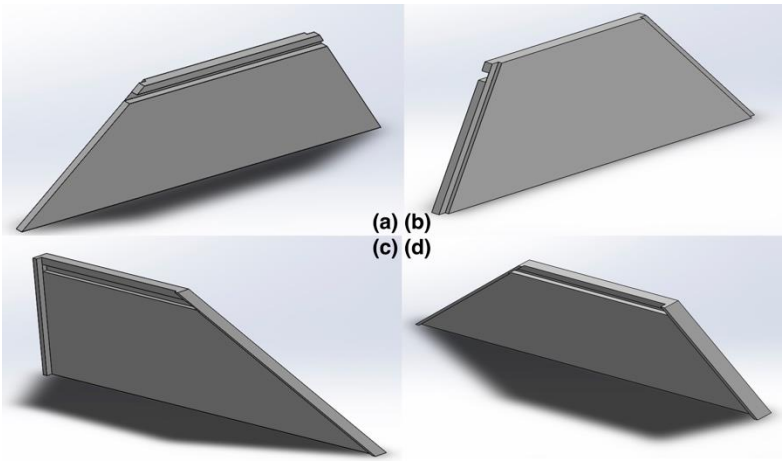

Figure 19. (a) back shield (b) front shield (c) left shield (d) right shield.

2.1.6 Shutter Mechanism

There are four basic components of the shutter mechanism: the tungsten shutter block, two tracks that the shutter moves on, and an air-piston/spring mechanism that drives the shutter. The student has modeled the mechanism for the most oblique additional pinhole for multiplexing. The complete picture is seen in Figure 20 below.

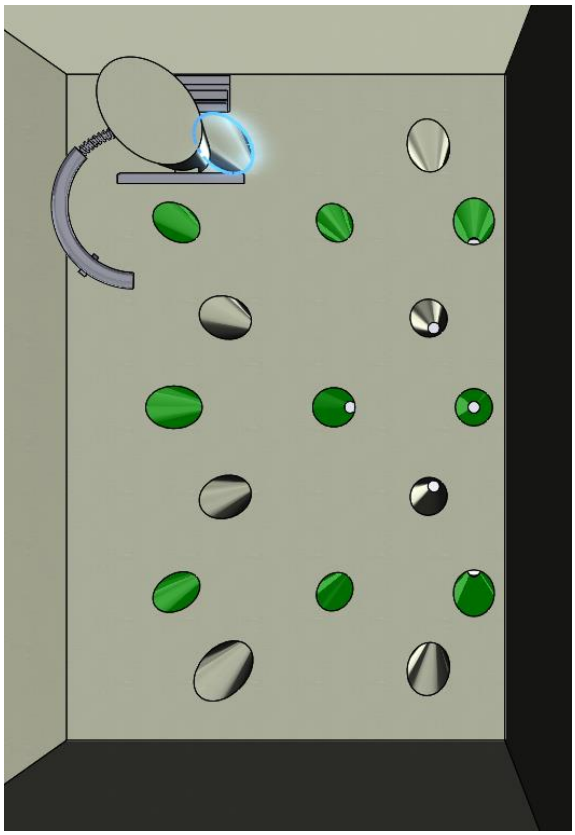

Figure 20. Bottom view of the aperture plate in the assembly showing the created shutter mechanism for the most oblique additional pinhole for multiplexing that is highlighted in blue.

2.1.6.1 Shutter Block

The isotropic view of the shutter block is seen in Figure 21 below. The two T-shaped extensions on the side allow the block to move on the tracks which will be discussed in the next

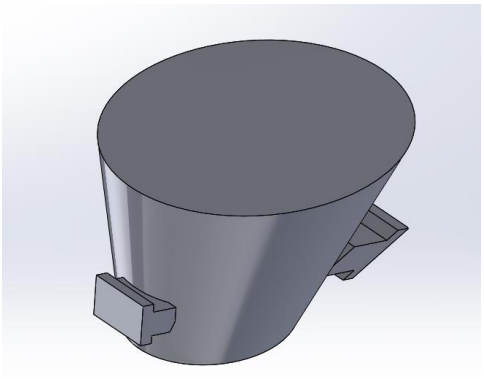

Figure 21. Isotropic view of the shutter.

section. The shutter block uses the same tungsten alloy as the collimator plate, and is essentially an extension of the corresponding pinhole but filled with actual material. This allows the complete blockage of photons traveling through the pinhole. It is demonstrated in Figure 22 below. The thickness has been determined so that when the shutter moves to the completely

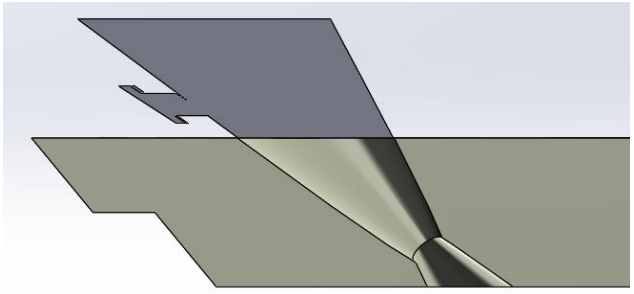

Figure 22. Cross-sectional view of the collimator plate and shutter. This view only shows one extension for the track because the extensions are not created on the same plane with each together due to the elliptical shape of the shutter.

open position it almost touches the back shield in order to allow all the photons through. The thickness is 1.6 cm which yields a penetration percentage of 3.47% for the 529 keV secondary photon emitted from the decay of I-123. Considering the low abundance of about 1% of these incident photons, the value is acceptable as the total probability is 3.47% of 1%.

2.1.6.2 Shutter Tracks

The shutter slides on two tracks whose geometries are illustrated in Figure 23. The pit portion has the same dimension as the extension of the shutter shown in Figure 24 below. Each track has two end walls that set the boundary that the shutter can move within.

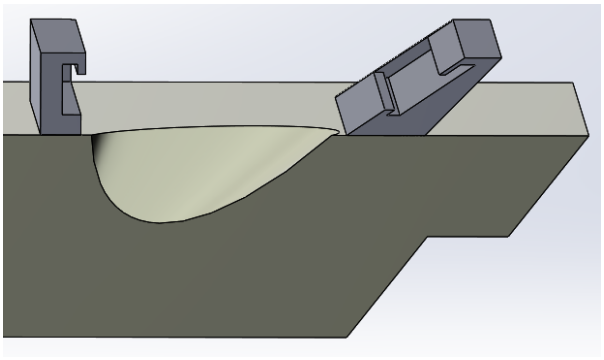

Figure 23. Cross-sectional view of the two shutter tracks.

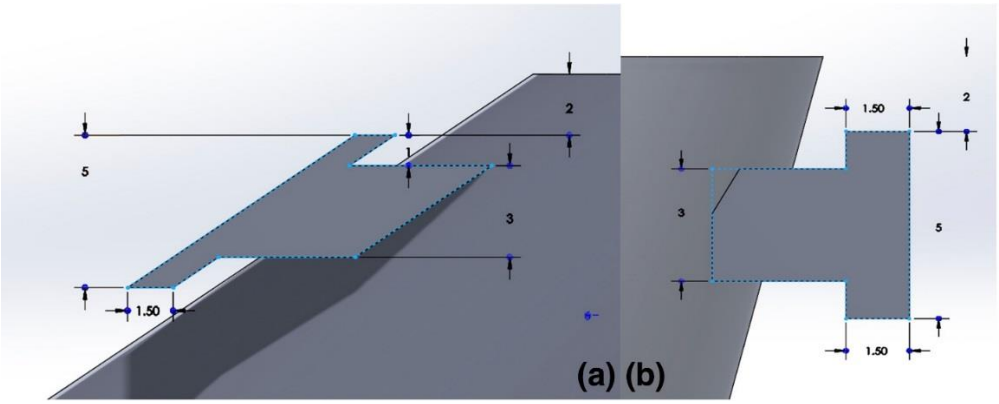

Figure 24. Dimension of the two shutter extensions which is replicated on the tracks.

2.1.6.3 Air-Piston/Spring Mechanism (Curved)

The mechanism consists of an air tube, air piston, and spring. It can be seen in Figure 25 below.

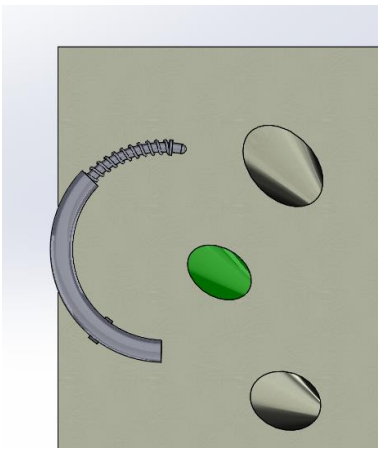

Figure 25. The bottom view of the collimator plate showing the air tube, the piston, and the spring.

When the spring is contracted and air is supplied from an air tank, the piston is pushed, moving the shutter to the right and stretching the spring. When the air supply is off, there is no force pulling the spring. As a result, the spring contracts automatically and pulls the shutter back to the original position. This can be seen in Figure 26 below.

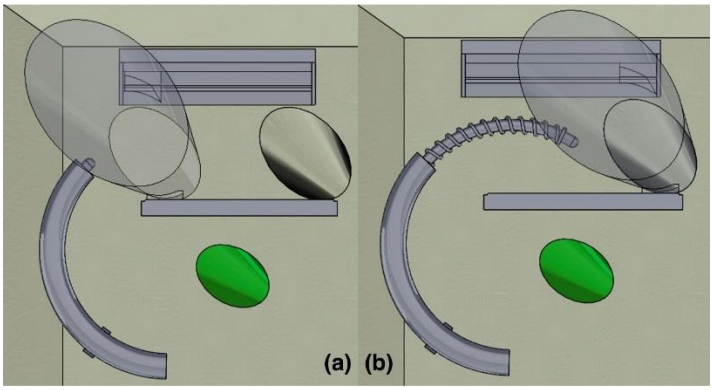

Figure 26. (a) Spring is contracted and the pinhole is open. (b) Spring is stretched and the pinhole is shut.

The air tube is a curved cylinder that follows the path of an arc. Figure 27 below shows the cross-sectional of the air tube. It is supported by two stands that secure the tube on the collimator plate. The spring is attached to the plate half way in the tube with air channels that allow air to pass through when the supplying air pushes the piston.

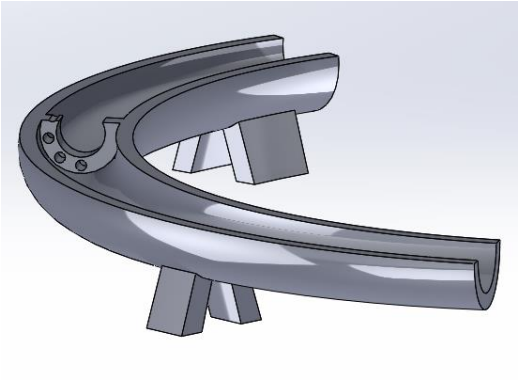

Figure 27. Cross-sectional view of air tube.

For the piston, shown in Figure 28 (a), to move back and forth in the tube, it has the same curvature as the air tube (based off of arcs of the same radius about the same center). The enclosed end in the shape of a cylinder is pushed by air and moves until it is stopped by the thin plate of the air tube. The moving end of the spring is attached to the plate close to the exposed end of the piston which is illustrated in Figure 28 (b).

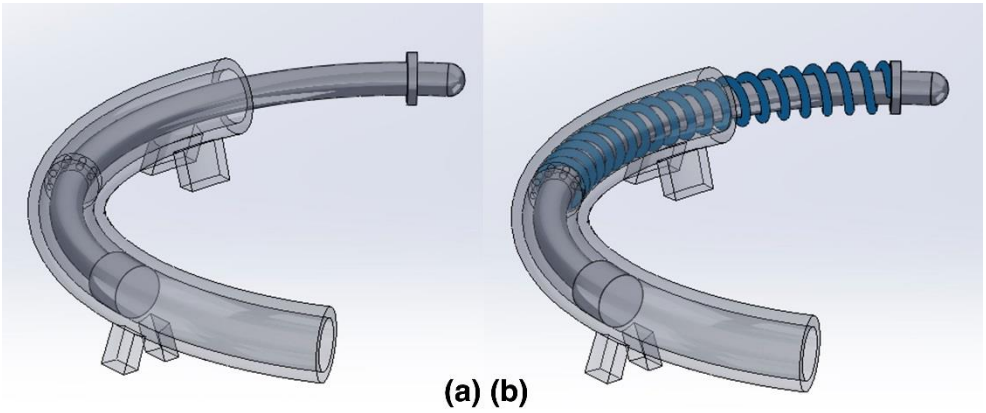

Figure 28. (a) Piston in the air tube (b) spring highlighted in blue.

2.2 Assembling Process

The collimator plate is first placed in the assembly. The crystal is placed 17.25 cm below the aperture level shown in Figure 29 below.

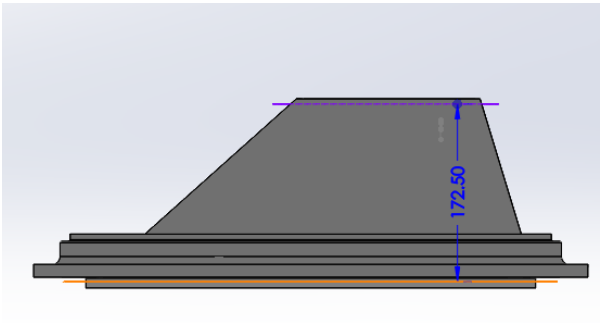

Figure 29. Side view of the MPH collimator demonstrating the distance from the crystal to the aperture level

The base is then placed 1 mm above the crystal top surface. In the side view, the front edge of the base keeps an approximate distance of 74 mm with the caudal edge of the imaging volume. "Thus it is the minimum axial extent of a patient's anatomy lost in brain imaging superior to the patient's shoulders, when the camera head just clears the shoulders during acquisition." (M. A. King, 2016) It can be seen in Figure 30 below. The four shields are then placed in an order so that they slide

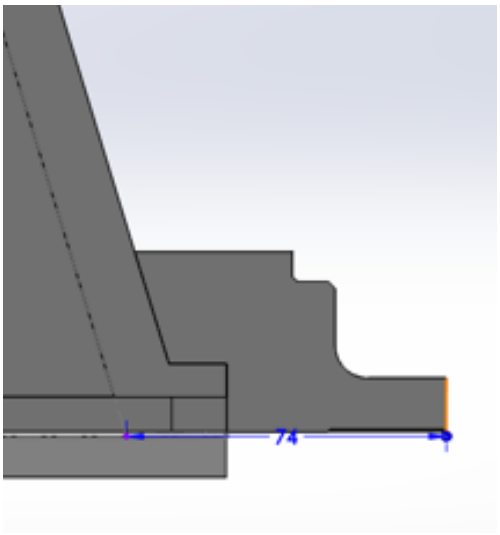

Figure 30. Cross-sectional view of the assembly

onto the collimator plate and eventually are able to hold each other. This is achieved through first sliding the front and back shields onto the collimator plate, and then "locking" the existing components by inserting the left and right shields. The two steps of the assembling process are illustrated in Figure 31 below. Now, in order for this pyramid structure to be attached with the

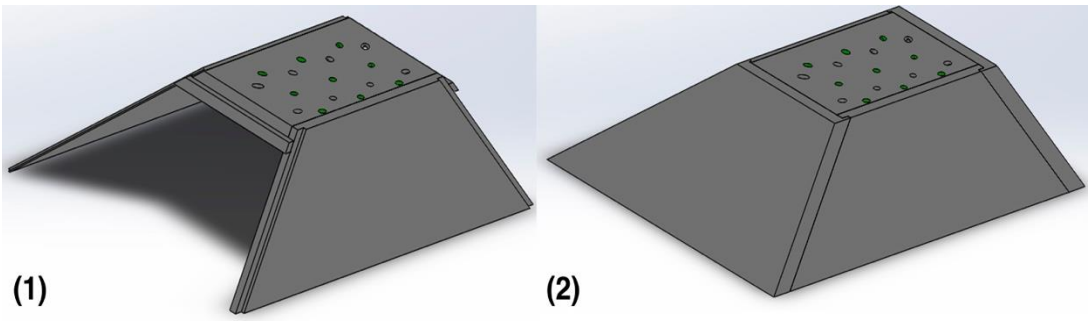

Figure 31. Assembly process of the collimator plate with the four shields (base and crystal not shown).

base, extra materials that extend from the bottom edge of each side shield are added to "grab" onto the base as seen in Figure 32 below. The axis of rotation (AOR) is then added axially on the system to act as the

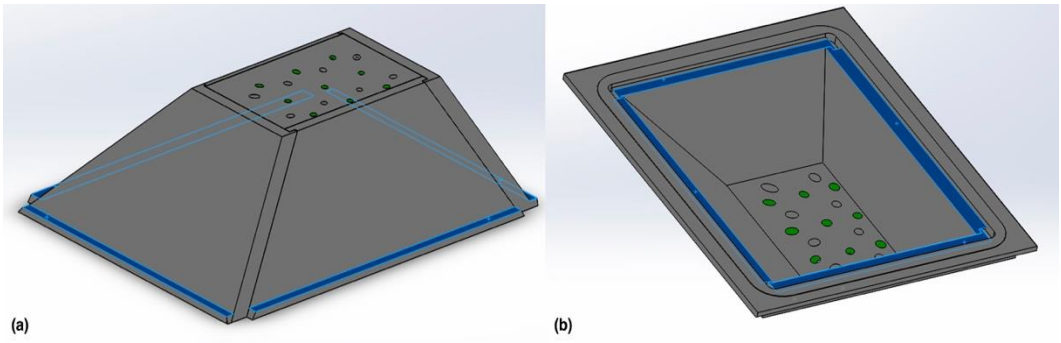

Figure 32. Side Skirts are highlighted in blue.

rotational axis that the collimator moves about to simulate the actual SPECT operating environment. The XCAT phantom is then placed where the center of the brain is at the same location as the VOI. The entire collimator system can be seen in Figure 33 below.

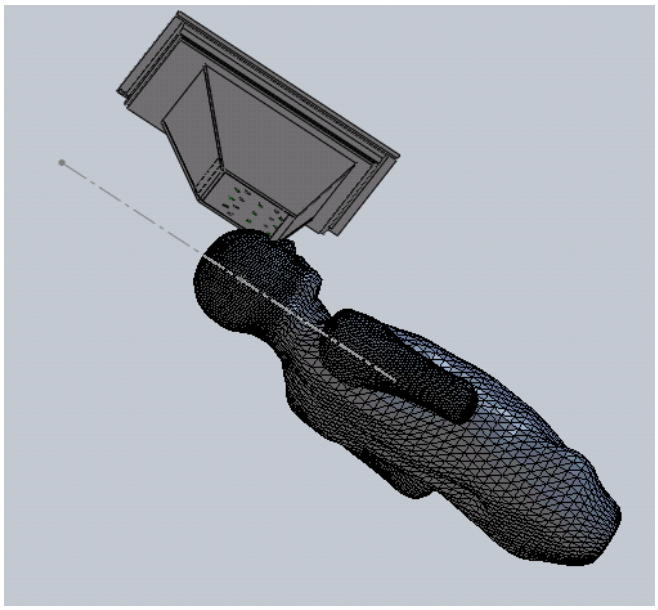

Figure 33. Complete view of the collimator system with XCAT phantom added. The dashed line indicates the axial direction of the phantom which is also what the MPH collimator rotates about.

2.3 Validation

2.3.1 Spatial Constraint

As the patient is injected with the imaging agent, the substance is spread throughout the body. In order to avoid photons penetrating the back shield outside the pinholes and registering on the detector, the back shield must be far enough from the direct pinhole which is directly underneath the striatum. We compared the distance between the striatum and the top of the head to the axial distance between the VOI (or direct pinhole location) to the back edge of the collimator plate. The data used for the human anatomy is obtained from the Department of Defense manual (Group, 2000). The eyes, an external indication of the lower bound for the center of the striatum, are 125 mm below the top of the head in ninety-nine percent of people. This number is well below the 157 mm axial distance between the direct pinhole to the back edge of the collimator plate as shown in Figure 34 below, indicating that the actual distance of interest is even less than 125 mm and safer because the striatum is above the eye level.

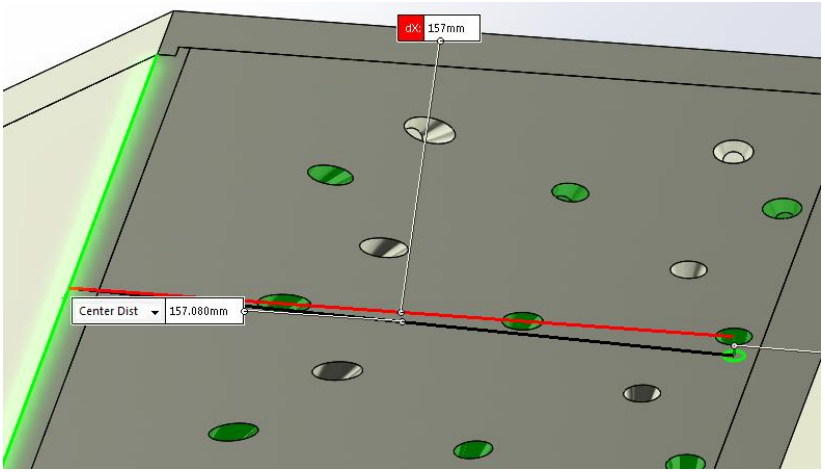

Figure 34. Distance between direct pinhole and the back end of the collimator.

In the assembly, the XCAT phantom provides a direct way of insuring there is no

collision between the MPH collimator and the patient, specifically at the nose and shoulder. The screenshots in Figure 35 below shows the result.

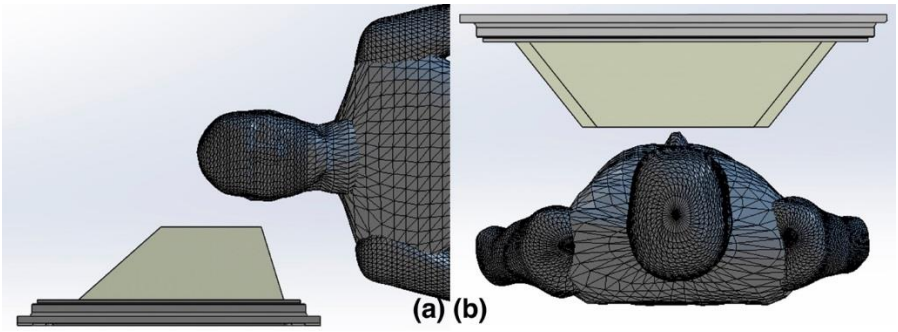

Figure 35. (a) Coronal view of the XCAT Phantom (b) Transverse view of the XCAT Phantom.

Adjustments of the MPH collimator geometry have also been made to accommodate the ability of the collimator being mounted on the collimator cart shown in Figure 36 below. The

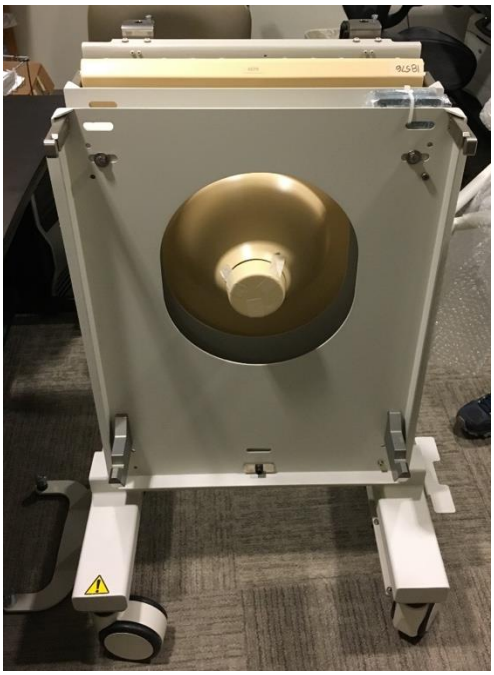

Figure 36. Collimator cart carrying the commercial single pinhole collimator.

main dimension of the collimator cart is measured in the clinic and a simple cart model is created

as the purple structure in Figure 37 (a). Its orientation with respect to the MPH collimator is replicated from the measured clinical orientation when it carries the commercial single pinhole collimator. Eleven millimeters above the center hole of the collimator cart, metal material starts to be used which needs to be avoided for the integrity of the cart. Therefore, adjustments to the geometry of the MPH collimator have been made to lower the interference to below 11 mm, and Figure 37 (b) shows the degree of interference in the current design.

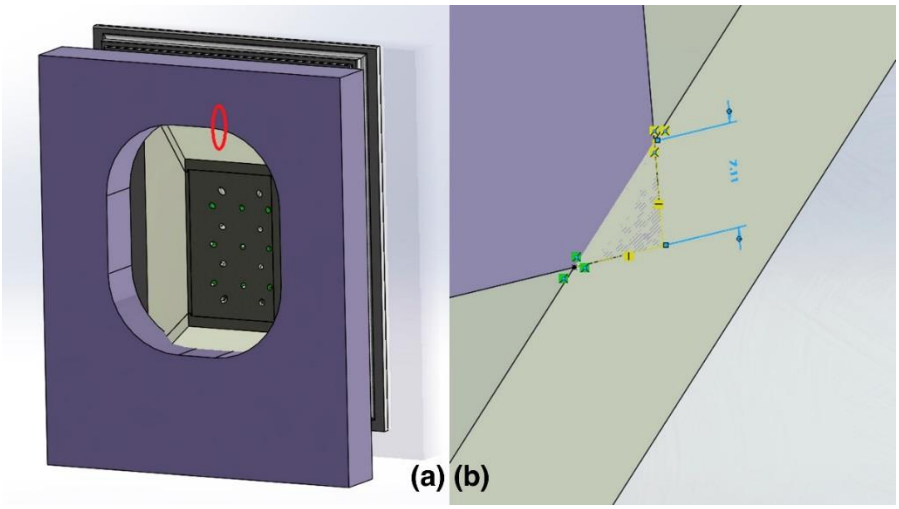

Figure 37. (a) Cart Mockup (purple) (b) intersection between the right shield of the MPH collimator and the collimator cart, highlighted in red oval in (a).

2.3.2 Weight Constraint

For the MPH collimator to operate accurately and to prevent system failure, the weight of the new camera should not exceed the weight of the current collimator which is 131 kg. The weight of the collimator plate, four side shields, and the collimator base together is 114.52 kg. When all the components in the shutter assembly are defined to be tungsten alloy (this is an overestimate as the components except the shutter itself do not have to be made of such heavy material), the weight of the assembly is less than 0.3 kg. Assuming the rest of the seven

assemblies have similar weight, the total weight of all the shutter mechanisms is 2.4 kg. Therefore, the total weight of the current model is about 117 kg which is about 90% of the current weight. Therefore, the weight is within the safety margin.

2.3.3 Deformation

In order to simulate material deformation at selected positions of the collimator head during operation, specimens made for tensile testing were machined to obtain the Young's Modulus of the material. Following the tensile testing standards of ASM International (Davis, 2004), a flat shape is chosen over a round shape to provide ease of manufacturing of the specimen for such a high-strength mixture. The selected specimen drawing is demonstrated in the Figure 38 below. Figure 39 shows the tested specimens and the untested ones.

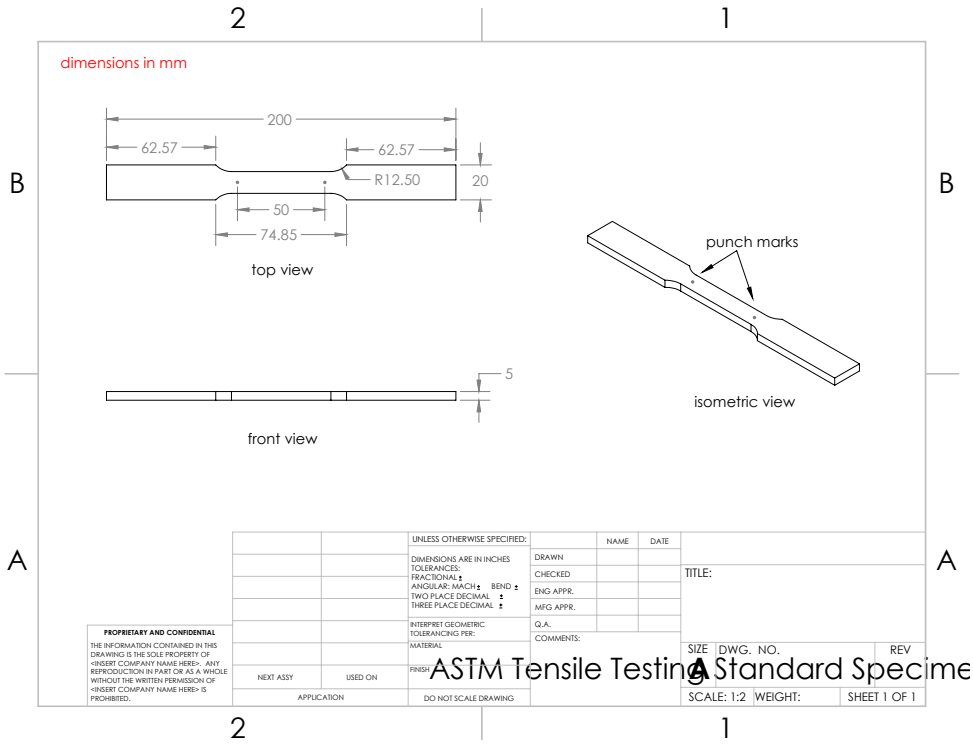

Figure 38. SolidWorks drawing of the tensile testing specimen design.

Figure 39. Two sets of specimens: tungsten alloy and lead alloy. For each set, the upper one is the tested and the lower one is the unused.

The student performed tensile testing at the civil engineering department of WPI for both materials. Four lead specimens labeled Pb_1, Pb_2, Pb_3, and Pb_4 and two specimens labeled W_1 and W_2 are tested and the obtained data is analyzed. The stress-strain graph for the two materials are shown in Figure 40 and Figure 41 below.

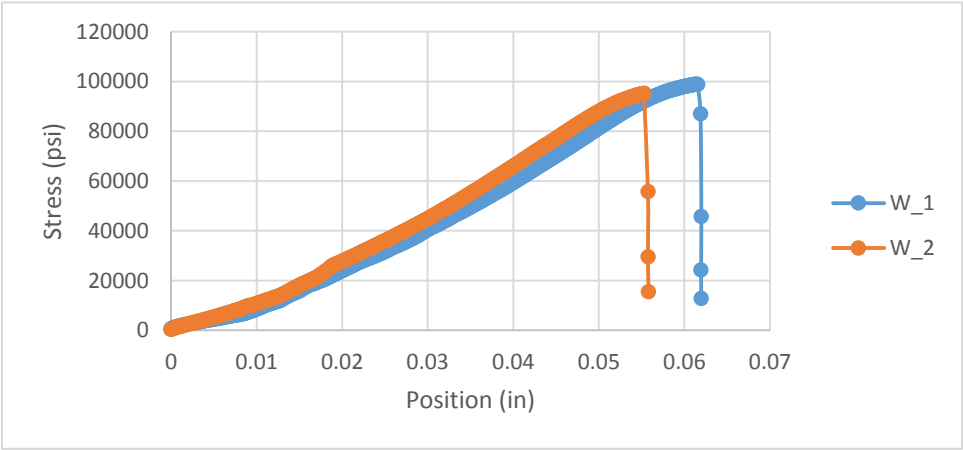

Figure 40. Stress-strain curve of two tungsten alloy specimens.

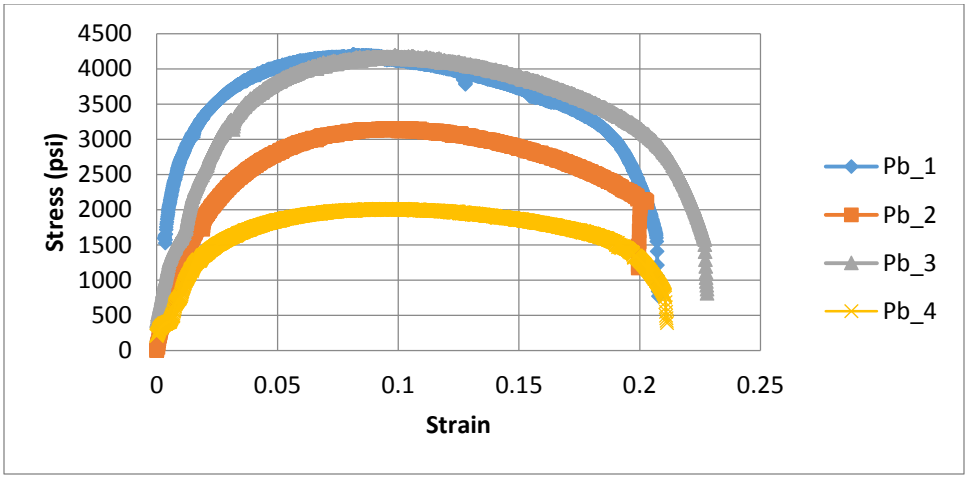

Figure 41. Stress-strain curve of four lead alloy specimens.

The same x range is chosen at a linear portion and the corresponding slopes were determined. These values are then used to produce the average young's modulus which are 1.97E5 for lead alloy and 19.81E15 psi for tungsten alloy. These values, however, do not agree with those provided by CES EduPack which are represented by ranges of 1.87~2.47E6 psi and 39.2~40.9E6 psi, respectively, making both tested values approximately a factor of 10 off. The testing procedure has been re-examined and no error can be determined. Nevertheless, given that the data for both materials are off in a similar fashion, one possible source of error is the setting of the machine that contributes to a conversion error. The group subsequently decided to have the remaining two lead alloy specimens tested at Westmoreland Mechanical Testing & Research, Inc. Results are shown in Figure 42 and Figure 43 below.

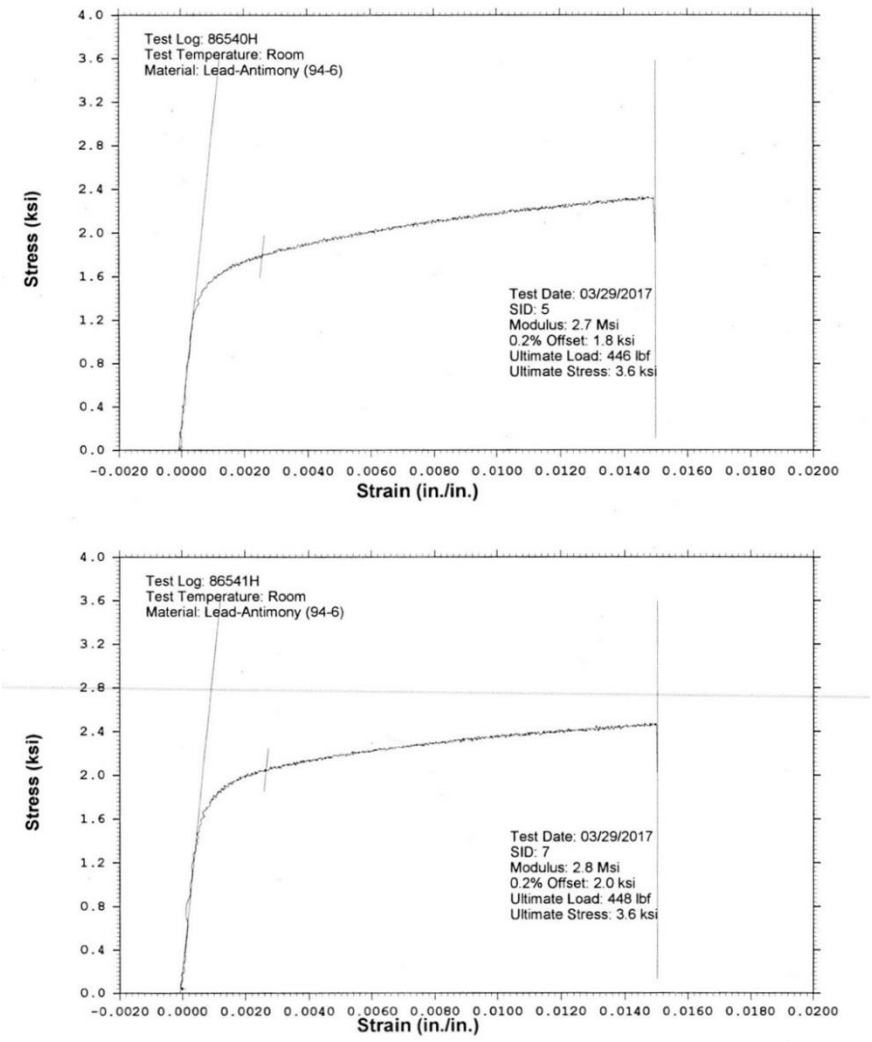

Figure 42. Stress-strain curve of tested tungsten alloy by the testing company.

Specimen ID	Testlog	Width (in)	Thickness (in)	Poisson's Ratio	Modulus (Msi)
5	86540H	0.4928	0.2522	0.4007	2.60
7	86541H	0.4930	0.2523	0.4108	2.60

Figure 43. Tested mechanical properties of the two specimens

From the report, the Young's modulus of 2.60 Mpsi fall into the range from CES EduPack. Therefore, the Young's modulus for the two materials obtained from this database are also chosen from CES EduPack.

According to the collimator drawing by Philips (confidential), the collimator is attached to a cover along the edges with epoxy and a set of screws on one edge through both the cover and the edge. However, the screws are temporarily ignored for simulation. If deformation is unacceptable, the screws will then be defined and another set of simulation will be performed.

Deformation simulation are performed in SolidWorks simulation. The attaching faces of the collimator base is defined to be fixed for the assumption that the collimator cover is a rigid driving component. Meshes used for FEA are chosen to be the coarsest and the direction of gravity is chosen based on the location of the collimator for each simulation because the collimator rotates about the patient in clinical settings. Simulation is performed when the collimator is at top, right (when facing the collimator), and bottom location. The results are provided in Figure 44, Figure 45, and Figure 46.

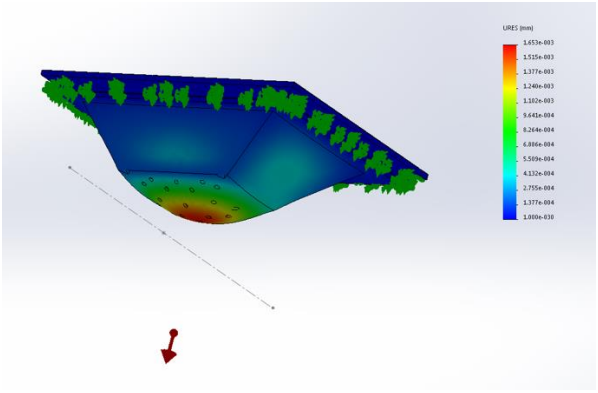

Figure 44. SolidWorks FEA simulation when the MPH collimator is at the top position.

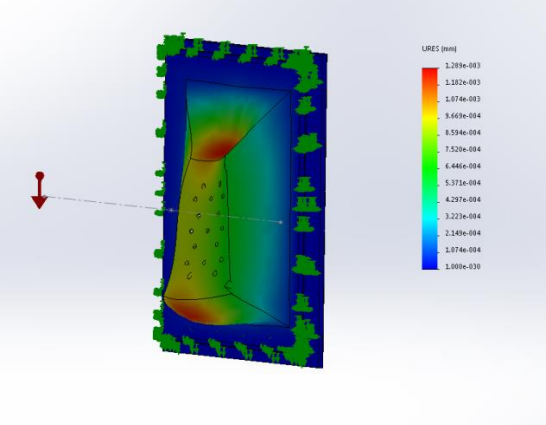

Figure 45. SolidWorks FEA simulation when the MPH collimator is at the right position.

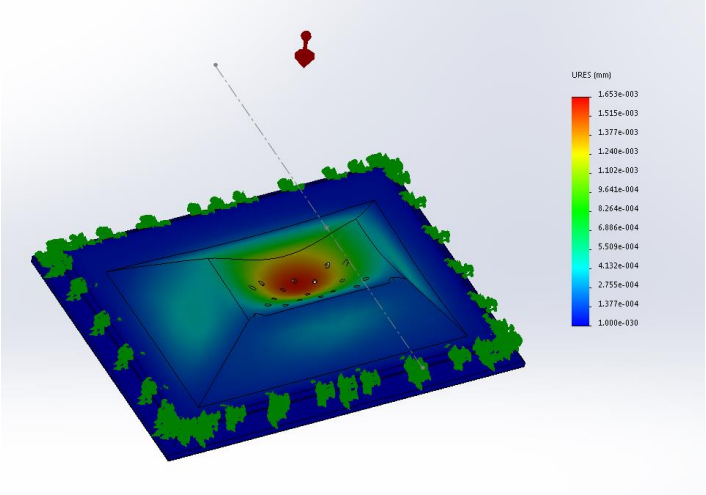

Figure 46. SolidWorks FEA simulation when the MPH collimator is at the bottom position.

The largest displacement (red) is on the scale of micrometer. Therefore, the system is determined to be stable.

2.3.4 GATE

The geometry of the MPH collimator (collimator plate and side shields), once completed, is imported into GATE using a plug-in. The model can be seen in Figure 47.

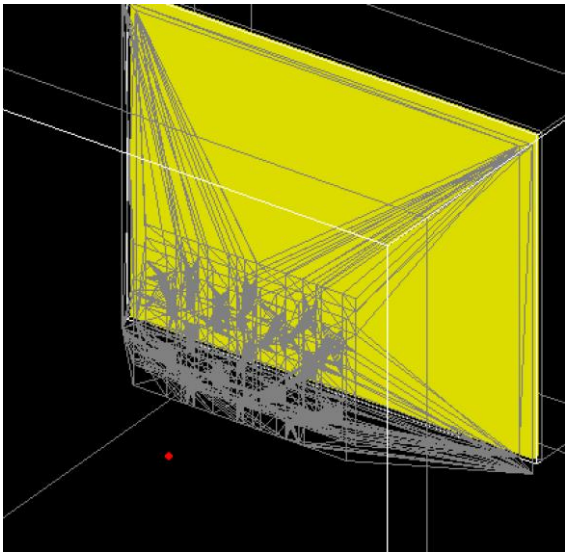

Figure 47. MPH collimator in GATE.

The XCAT Phantom (not visualized in GATE) with I-123 defined to be distributed in the striatum is placed at the VOI, the same position as the SolidWorks assembly. Figure 48 below demonstrates the simulation result using the geometry of the current MPH collimator.

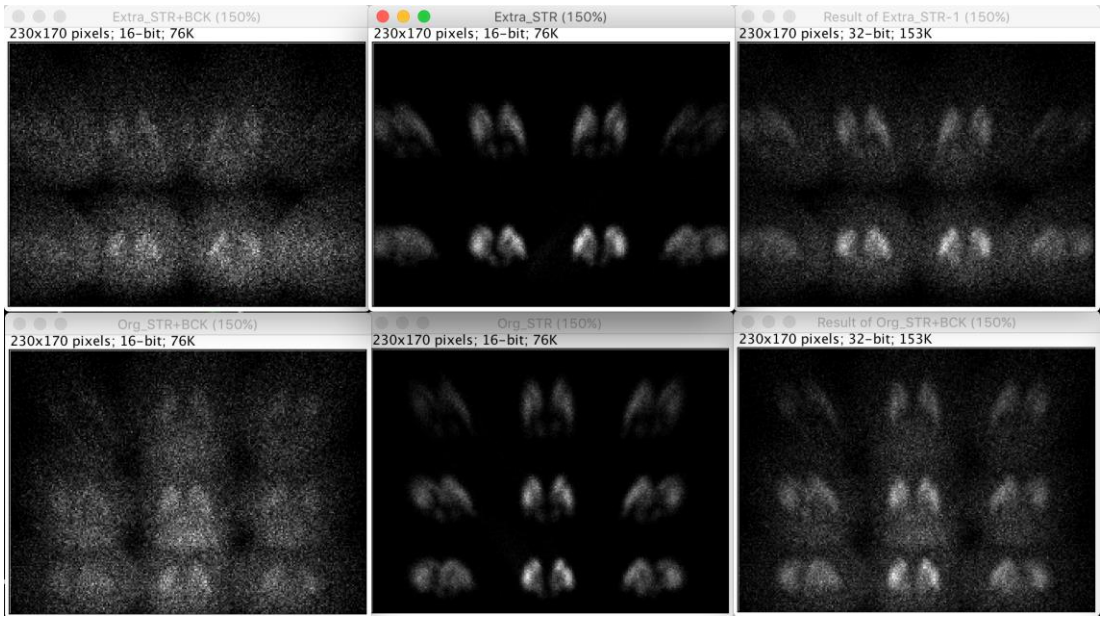

Figure 48. GATE simulation result of the additional eight pinholes for multiplexing (top three) and the original nine pinholes (bottom three).

The top and bottom three pictures each demonstrate the simulation with the additional eight pinholes for multiplexing and the original nine pinholes. The images in the first column are acquired with the entire brain including the striatum and the rest of the brain as the background. The images in the second column are acquired with only the striatum as the object with counts of ten folds compared to those in the first column. The third column demonstrates the result from overlapping the images of the first two columns.

Figure 49 below shows the simulation with both original and additional sets of pinholes open, forming the case of multiplexing. The image on the left includes the background and the

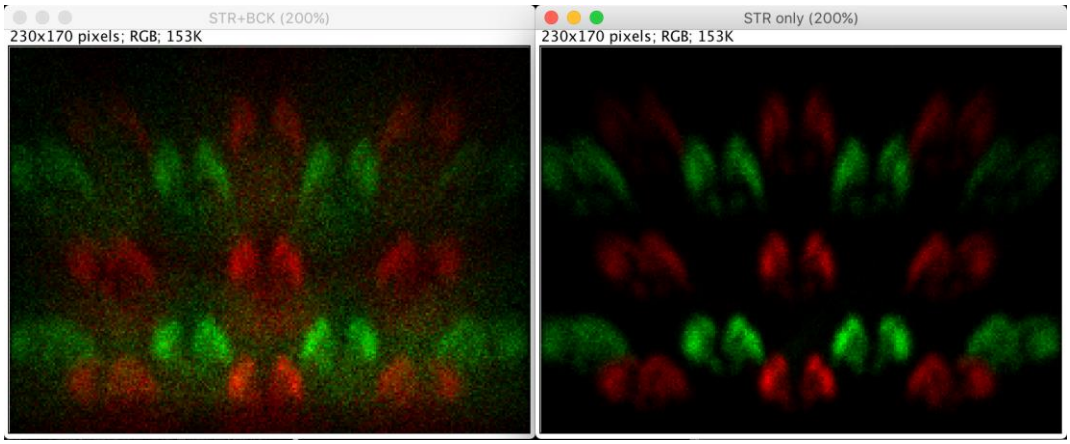

Figure 49. GATE simulation results for multiplexing, red: original nine pinholes & green: additional eight pinholes.

image on the right does not. It is clear to see that there are overlapping regions in the left image but the projections of the critical structure, striatum, are not intersecting with each other in the right image. This minimizes potential artifacts during the reconstructing of the striatum.

3 Conclusion

In this project, an MPH collimator assembly is modeled in SolidWorks to replace the current single pinhole collimator. Spatial, mechanical, and deformation constraints are met and photon penetration with Monte-Carlo simulation is also performed with GATE to simulate the actual SPECT environment. The project will continue during the summer of 2017.

4 Discussion

4.1 Component Attaching Process

The current model only geometrically places the components together without any space in between. However, specific plan is needed determine how to actually attach each component for the final stage of the research when the system is being assembled as indicated in Figure 50. Possible methods include epoxy and tungsten screws. SolidWorks simulation is recommended be used again here.

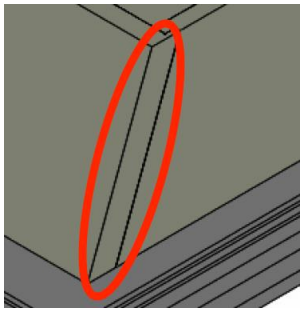

Figure 50. One attaching surface.

4.2 Shutter Mechanism

Currently, the moving end of the spring is attached to the piston tip. During contraction, it pulls only the piston back rather than the shutter as well. Due to the curvature of the spring, the moving end of the spring does not move in a linear trajectory with the direction that the shutter moves in as shown in Figure 51. This makes it impossible to attach the moving end of the spring

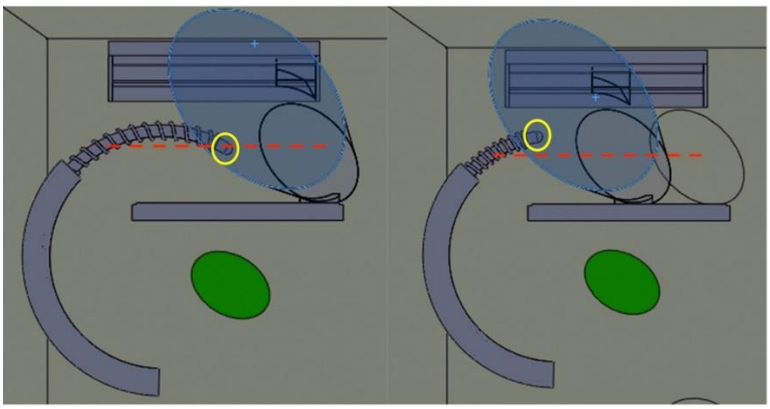

Figure 51. The change of relative position of the piston tip with respect ot the track direction of the shutter.

directly to the shutter which will change the shape of the spring and cause collision between the spring and the piston that the spring wraps around. Therefore, one possible solution is to attach the piston to the shutter through a connecting joint. The proposal is to add a hook on the tip of the piston and, at the same level, a round bar that extends out from the surface of the shutter that the hook is hooked onto. This allows the piston to slides and pull/push on the shutter at the same time. The setup should work similar to a car hook.

In terms of photon passage, it is recommended to check if the lower track of the current shutter at the most oblique pinhole can potentially block photons through the additional pinhole one row down as shown in Figure 52 below.

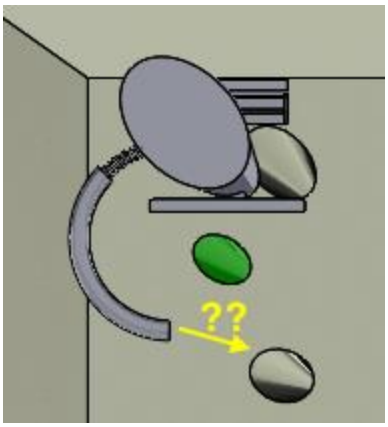

Figure 52. Potential blockage of the adjacent pinhole by the air piston.

For the first column of the additional pinholes that are closer to the direct pinhole as circled in Figure 53 the proposed shutter design is aligned with that created for the direct pinhole as Figure 54 shows.

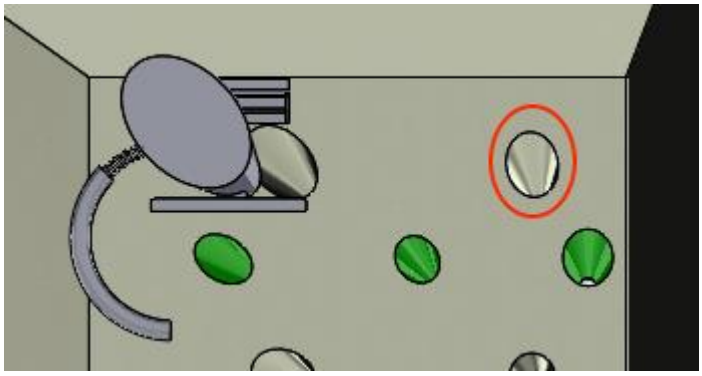

Figure 53. The other additional pinhole of the same column circled in red.

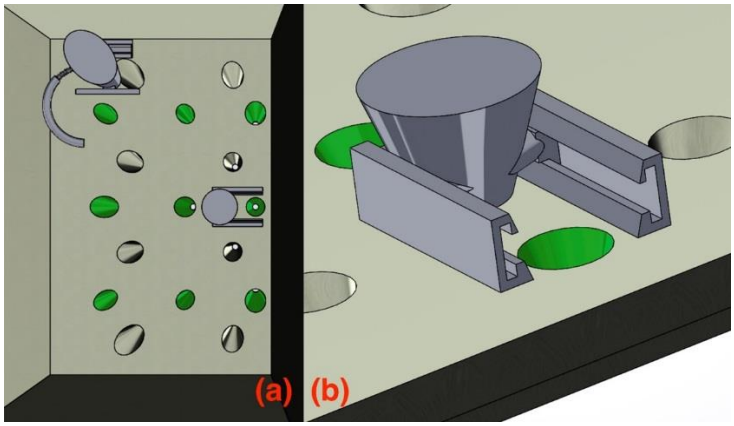

Figure 54. Shutter for the direct pinhole (a) top view with the entire collimator plate shown (b) isotropic view.

4.3 GATE Result

The result in GAETE simulation produces a low count error at one of the most oblique pinholes for both sets of the original and additional pinholes as shown in Figure 55 below.

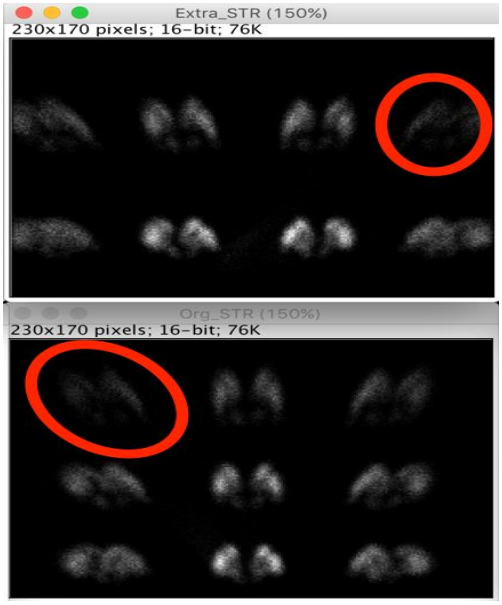

Figure 55. Low count issue in GATE circled in red.

This can also be seen with a point source for the additional eight pinholes as Figure 56 demonstrates.

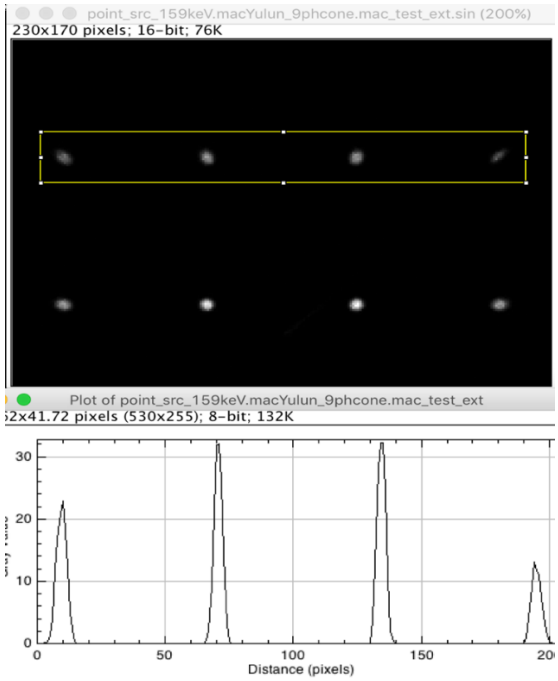

Figure 56. GATE simulation result of the additional pinholes with a point source. The chart in the lower image demonstrates the counts at the corresponding pinholes from the region selected in the yellow rectangle in the upper image.

The student then simulates with a previous model of a full rectangular plate with only the original nine pinholes created as seen in Figure 57 (a) and its simulation result is seen in Figure 57 (b).

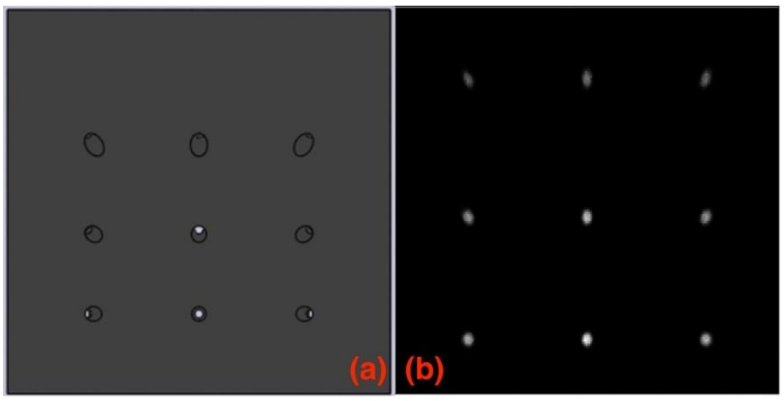

Figure 57. (a) Previous model of only original pinholes (b) GATE image of the model.

The result does not indicate any low count issue especially at the most oblique pinholes. In order to find out the error, the symmetry of the pinholes (the left most column is mirrored

from the right most column) has been checked in the current model and such geometric requirement is satisfied. Other strategies such as only simulating the plate and covering a selection of the total pinhole set have all failed to identify the source of error. One possible answer to this is that the SolidWorks model has become corrupted for meshes. Because the geometry in SolidWorks is structured as meshes, the creation of the additional pinholes overwrites and distort the symmetry of the meshes. This is demonstrated in Figure 58. This may also be caused during the process of file conversion from SolidWorks into GATE.

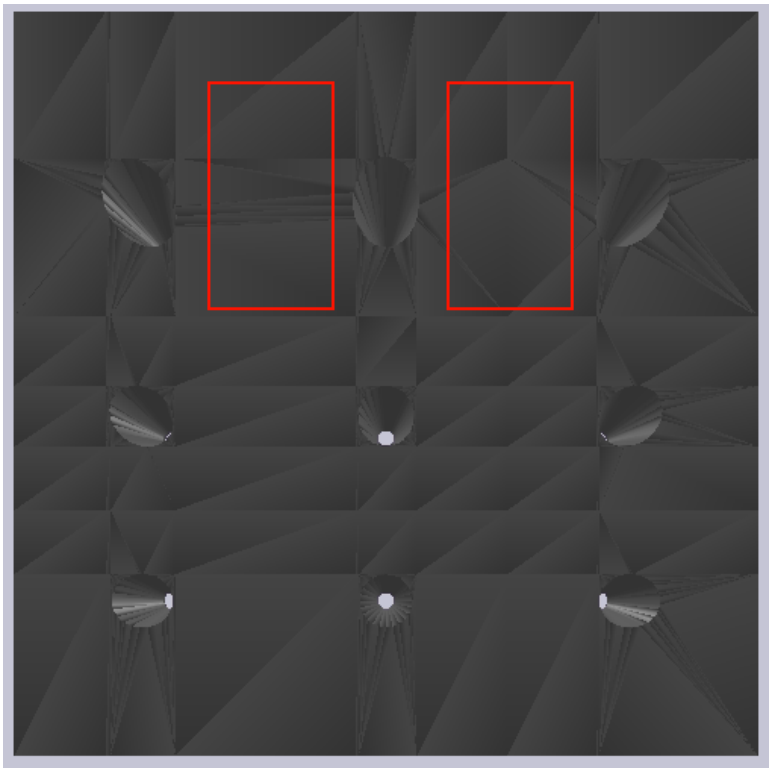

Figure 58. Potential unsymmetrical meshing.

5 References

Cécile Chaix, S. K. (2015). Integration of AdaptiSPECT, a small-animal adaptive SPECT imaging system. *Proc SPIE Int Soc Opt Eng.*

Challenged, N. (2015, Dec 23). *2-Minute Neuroscience: Substantia Nigra*. Retrieved from https://www.youtube.com/watch?v=JJ6YB4674GQ

Conditions, N. C. (2006). *Parkinson's disease: national clinical guideline for diagnosis and management in primary and secondary care.* Suffolk: Royal College of Physicians.

David A. Weber, K. F. (1989). *MIRD Tables.* New York: Society of Nuclear Medicine.

Davis, J. (2004). *Tensile Testing Second Edition.* Materials Park,: ASM International.

Defense, D. o. (n.d.). Human Engineering Design Data Digest.

Giuliano Mariani, L. B. (2010). A review on the clinical uses of SPECT/CT. *European Journal of Nuclear Medicine and Molecular Imaging*, 1959–1985.

Group, D. O. (2000, April). Human Engineering Design Data Digest. Washington, DC.

Karen Van Audenhaege, R. V. (2015). Review of SPECT collimator selection, optimization, and fabrication for clinical and preclinical imaging. *Medical Physics, 42*(8), 4796-4813.

M. A. King, J. M. (2016). Design of a Multi-Pinhole Collimator for I-123 DaTscan Imaging on Dual-Headed SPECT Systems in Combination with a Fan-Beam Collimator. *IEEE Transactions on Nuclear Science, 63*(1), 90-97.

News, I. T. (2016, July 25). *UltraSPECT Xpress3.Cardiac Installed at Four RWJPE Locations*. Retrieved April 19, 2017, from https://www.itnonline.com/content/ultraspect-xpress3cardiac-installed-four-rwjpe-locations

Philips. (2017). *BrightView XCT SPECT/CT system*. Retrieved April 15, 2017, from https://images.philips.com/is/image/PhilipsConsumer/HC882482-RTP-global-001?wid=4000&hei=4000&fit=constrain&fmt=jpeg&qlt=100,1

S Jan, e. a. (2004). GATE: a simulation toolkit for PET and SPECT. *PHYSICS IN MEDICINE AND BIOLOGY, 49*, 4543–4561.

Simon R. Cherry, J. A. (2012). *Physics in Nuclear Medicine.* Philadelphia: Saunders.

Technology, N. I. (n.d.). *Element/Compound/Mixture Selection*. Retrieved April 16, 2017, from http://physics.nist.gov/PhysRefData/Xcom/html/xcom1.html

Turner, J. E. (2007). *Atoms, Radiation, and Radiation Protection.pdf.* Oak Ridge, TN, USA: Wiley-VCH.

W. P. Segars, G. S. (2010, September). 4D XCAT Phantom for Multimodality Imaging Research. *Medical Physics, 37*(9), 4902–4915.